From chaotic spin dynamics to noncollinear spin textures in YIG nanofilms by spin-current injection

Henning Ulrichs*

I. Physical Institute, Georg-August University of Göttingen, Friedrich-Hund-Platz 1, 37077 Göttingen, Germany

(Received 10 July 2020; revised 21 September 2020; accepted 3 November 2020; published 16 November 2020)

In this paper I report on a numerical investigation of nonlinear spin dynamics in a magnetic thin film made of yttrium iron garnet (YIG). This film is exposed to a small in-plane oriented magnetic field and strong spin currents. The rich variety of findings encompasses dynamic regimes hosting localized, nonpropagating solitons, as well as a turbulent chaotic regime, which condenses into a quasistatic phase featuring a noncollinear spin texture. Eventually, at the highest spin current, a homogeneously switched state is established.

DOI: 10.1103/PhysRevB.102.174428

I. INTRODUCTION

Recent advances [1–5] in the art of thin-film growth allow us nowadays to prepare yttrium iron garnet (YIG) films with nanometer thickness. These films in particular feature magnetic losses comparable to or lower than metallic ferromagnets like the widely used permalloy or amorphous CoFeB alloys. Such YIG nanofilms are of great interest to implement functionalities based on wave interference in magnon spintronic applications [6–9]. Being electrically insulating, YIG allows us to completely disentangle spin and charge current related physics. This makes this material in particular attractive for studies on spin-related transport phenomena [10–16]. In addition to its appearance in these topical research fields, YIG has been, since its discovery, a great medium to study highly nonlinear spin dynamics. Turbulence [17], parametric instabilities [18–21], and even Bose-Einstein condensation (BEC) [21–23] have been studied in YIG for quite a few decades. But so far many of these intriguing phenomena could be realized only on rather macroscopic scales, rendering them less attractive for practical applications. To address these effects, YIG samples are usually exposed to strong, monochromatic microwave radiation, whose magnetic part can directly drive magnetization dynamics.

On the other hand, if single-frequency excitation is not a prerequisite, spin currents can be considered a convenient method for realizing broadband excitation. Spin currents can be generated by a charge current when they are led through a spin-Hall material [24–27]. These are, for example, the very common heavy metals platinum and tungsten. In a simple picture, one can relate the appearance of spin currents in patterned films consisting of these materials to spin-orbital coupling (SOC). If a lateral charge current carried by *a priori* non-spin-polarized electrons experiences scattering with SOC, this scattering gives rise to a vertical spin imbalance. This imbalance builds up between the top and bottom surfaces of the conducting film. When deposited on top of a YIG nanofilm, the spin accumulation at the interface can interact with the magnetic moments in the YIG. This in particular can result in an effective reduction of magnetic losses of magnons. A critical current can, in this context, be defined as the magnitude at which the mode with the lowest losses reaches the point of full damping compensation. The spin-current-induced instability of a particular mode is the essential mechanism behind spin-Hall oscillators, which have been realized with metallic permalloy [28,29], as well as with insulating YIG [30,31], as active magnetic media.

The findings presented in the following in particular shed light on the question of what happens if one exceeds the instability threshold in a situation when the injection of spin currents is confined to one lateral dimension or even not at all. Thus, the investigations presented here complement recent findings [12,14,15] about magnon transport phenomena in YIG nanofilms and theoretical investigations that predict BEC in such an experimental situation [32,33]. The micromagnetic approach applied here provides a view inside the film, circumventing spatial and temporal resolution limitations encountered in common experimental approaches like Brillouin light scattering [34], which is used to image magnetization dynamics. When confining the spin current, I have found first the nucleation of so-called spin-wave bullets, whose density quickly increases, leading to a chaotic regime. At even larger spin current a novel quasistatic phase condenses from these turbulent fluctuations. This phase is characterized by a stripelike, noncollinear magnetization texture. At higher current, this texture gradually disappears, and a fully switched, homogeneous magnetic state is established.

The rest of this paper is organized as follows. First, I provide details about the numerical method. In particular, I explain how I take temperature-related effects into account. Then, I present results obtained for the case of confined spin-current injection. After that, I present the findings for the case of unrestricted injection. In the final discussion, I explain the magnitude of the numerically found threshold current density, and I explain why turbulence arises. Finally, I present a tentative interpretation for the emerging quasistatic texture.

II. EXPERIMENTAL DETAILS

To simulate the spin-current injection into a YIG nanofilm with a thickness of $t_{\mathrm{YIG}} = 20\,\mathrm{nm}$, the micromagnetic

*hulrich@gwdg.de

simulation code MUMAX3 [35] was used. In this finite-difference numerical code, the magnetic film is divided into rectangular cells that are $5 \times 5 \times 20\,\mathrm{nm}^3$. Each cell hosts a magnetic moment with a fixed vectorial length, interacting by micromagnetic exchange and dipolar fields with its surroundings. A total lateral area of $2560 \times 2560\,\mathrm{nm}^2$ was considered. For the YIG film at 285 K, a saturation magnetization of $M_0 = 0.11\,\mathrm{MA/m}$, an exchange constant of $A = 3.7\,\mathrm{pJ/m}^2$, a gyromagnetic ratio of $\gamma = 1.7588 \times 10^{11}\,1/\mathrm{Ts}$, and a Gilbert damping constant of $\alpha = 0.001$ were assumed. The spin torque generated by the spin-Hall effect in a $t_{\mathrm{Pt}} = 3.5\,\mathrm{nm}$ thick Pt layer was taken into account by adding the Slonczewski torque term [36,37] to the equation of motion of the magnetization. As a conversion factor between charge and spin currents, a spin-Hall angle of $\theta_{\mathrm{SHE}} = 0.11$ and an interface transparency of about $\tau_i = 0.47$ were employed. These material parameters resemble typical experimental values, as used in [15]. The MUMAX3 script file in the Supplemental Material [38] provides all information to reproduce the simulations.

Note that I did not consider the Oersted field created by the charge current. In the Supplemental Material [38], I show that, due to its small magnitude, the Oersted field does not influence the dynamics. In contrast, the influence of sample temperature on the magnetization and exchange, enhanced by Joule heating, is taken into account. For simplicity, I have assumed homogeneous heating. Laterally inhomogeneous temperature profiles do not affect the dynamics, as discussed in the Supplemental Material [38]. In the simulation, a static reduction of the magnetization and temperature-driven fluctuations implemented by means of a fluctuating thermal field [35] are taken into account. The method is described in what follows. I assume the temperature dependence of the magnetization shown in Fig. 1(a), which was published in [39]. Note that these data are well described by a phenomenological power law with an exponent of 0.511(5) (red curve). Figure 1(b) shows experimental temperature calibration data from [15], which extrapolate quadratically (red curve) to $T_C = 560$ K at about $j = 8 \times 10^{11}\,\mathrm{A/m}^2$. Combining both data sets and fitting curves, I have constructed the current dependence of the magnetization shown in Fig. 1(c). This curve is taken for rescaling the effective magnetization at a given current and temperature in the simulation. This means that in practice the length of the magnetization vector in each simulated cell is adjusted accordingly. Note that in the simulation long-range, low-frequency fluctuations are included, stochastically excited by the thermal field. Such fluctuations further reduce the effective magnetization. Across the whole temperature range (285 to 560 K) valid here, I have found it necessary to increase the magnetization by about 1% to take the additional reduction of the effective magnetization by such fluctuations into account. For the exchange constant, I have assumed the classical micromagnetic expectation $A(T) \propto M_0(T)^2$ [40,41]. The resulting current dependence is shown in Fig. 1(d).

Figure 2 shows the experimental sample designs considered in this work. In Fig. 2(a), the case of a spatially confined spin-current injection is depicted, realized by patterning the charge current carrying Pt layer to a stripe with a width of $w = 500\,\mathrm{nm}$. In the simulation, the Pt stripe is considered only implicitly by enabling the Slonczewski torque only in the injection region beneath the conductor. Absorbing boundary

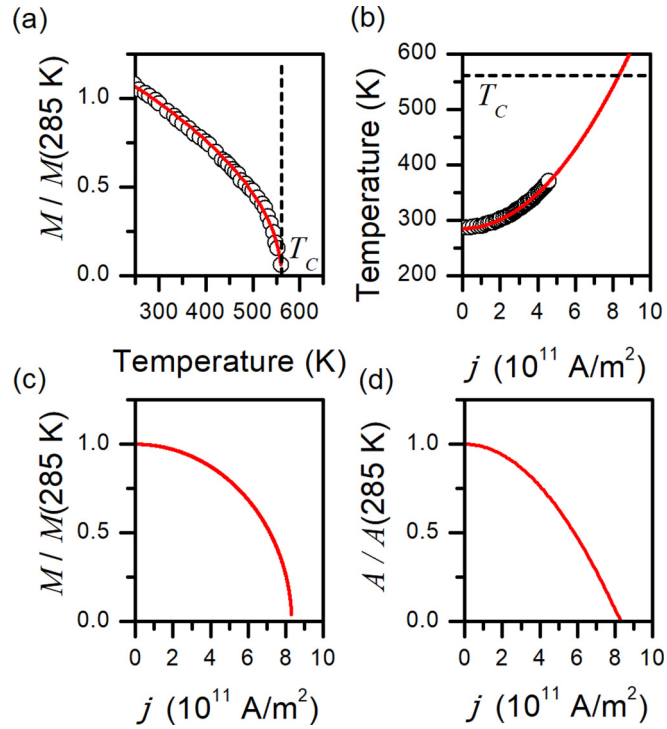

FIG. 1. Influence of Joule heating on static and dynamic magnetization. (a) Temperature dependence of magnetization according to [39]; the solid line is a power law fit. The dashed vertical line marks the Curie temperature T_C. (b) Current density dependence of the temperature underneath the Pt stripe according to [15]; the solid line is a quadratic fit. The dashed horizontal line marks the Curie temperature T_C. (c) Derived current density dependence of magnetization M_0. (d) Derived current density dependence of the exchange constant A.

conditions were applied to the edges parallel to the wire, and periodic boundary conditions (PBCs) were applied to the perpendicular edges. Therefore, an infinitely long wire was simulated. The external field had a magnitude of $\mu_0 H = 50\,\mathrm{mT}$, and it was oriented in the film plane, perpendicular to the wire. The detection stripe included in Fig. 2(a) is depicted to graphically define the region underneath the YIG film. This region is used for probing dynamics outside the actively excited region. In Fig. 2(g) the case of homogeneous spin-current injection is depicted. Here, the PBCs are applied to all edges.

III. RESULTS

Figure 2 depicts snapshots of the dynamics obtained for the two cases of confined and unrestricted spin-current injections, at current densities above and below a certain critical threshold j_{th}. Note that I quantify this threshold later from the data and use it to define the overcriticality Γ by

$$\Gamma = \frac{j}{j_{\mathrm{th}}} - 1. \tag{1}$$

A. Confined spin-current injection

Let us begin the inspection of the results by analyzing the case of spin-current injection confined to a stripe.

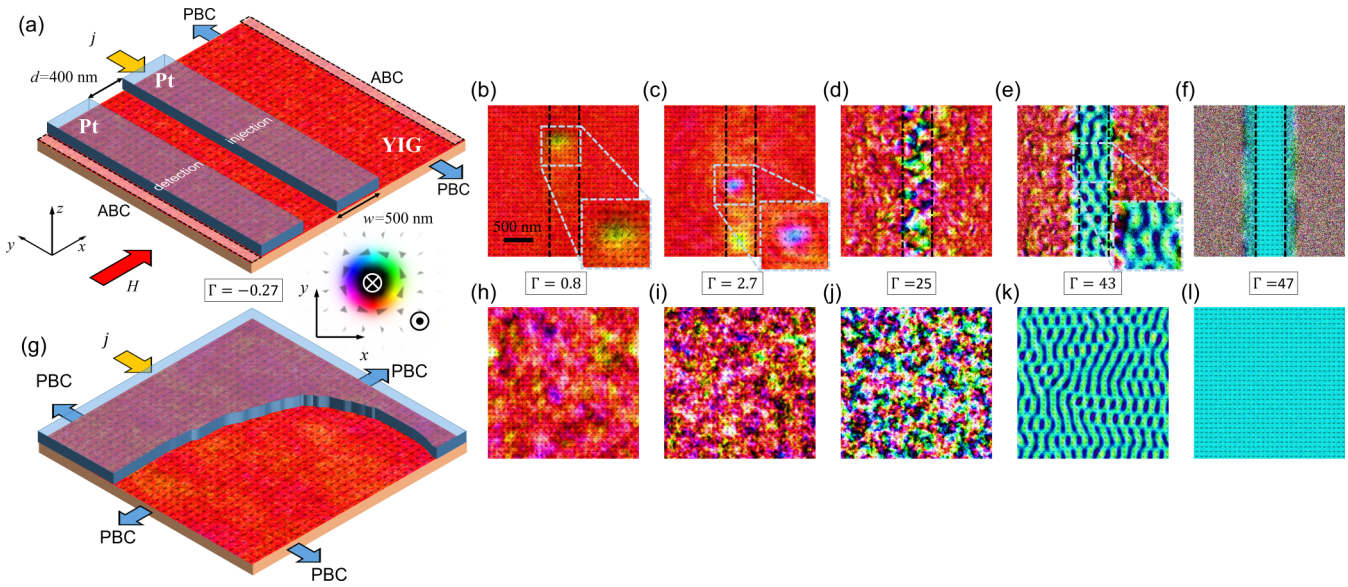

FIG. 2. Sketch of the experimental situations and snapshots of simulated magnetization dynamics in terms of the normalized magnetic vector field $\mathbf{m}(x, y)$. (a) Sketch for confined spin-current generation and injection. (g) Sketch for homogeneous spin-current generation and injection. Edges marked by PBC and ABC refer to periodic and absorbing boundary conditions. Note that both sketches include color-coded maps of $\mathbf{m}$, referring to a current density below the onset of bullet formation, at $\Gamma = -0.27$, as indicated. (b)–(f) Snapshots of $\mathbf{m}$ for increasing Γ as indicated for the case of confined spin-current injection. Dashed lines mark the boundaries of the Pt stripe. (h)–(l) Analogous snapshots of $\mathbf{m}$ for unconfined spin-current injection.

Figures 2(a) to 2(f) show snapshots of the magnetization after dynamic equilibrium has been established. For a current density below a certain threshold $j < j_{\mathrm{th}}$ [$\Gamma < 0$, see Fig. 2(a)], no dynamic response can be seen. When the current is increased to $j > j_{\mathrm{th}}$ ($\Gamma > 0$), this situation changes. Now, the simulation features localized hot spots, where the film is strongly excited [see Fig. 2(b)].

The normalized magnetization component $m_y^i = \frac{\langle M_y \rangle_{\mathrm{injection}}}{M_0}$ averaged across the injection area provides quantitative access to these dynamics. A representative time series obtained at $\Gamma = 7$ is shown in Fig. 3(b). The Fourier transform power spectrum shown in Fig. 3(c) is dominated by a strong peak at frequency $f_b = 2.4\,\mathrm{GHz}$. Note that this value is lower than the bottom of the linear spin-wave spectrum at about $f_0 = 2.7\,\mathrm{GHz}$ [dark blue dashed line in Fig. 3(c)]. Both spectral and spatial features are typical for so-called spin-wave bullet modes [42]. Such a bullet is a nonlinear, nonpropagating solitonic solution of the gyromagnetic equation of motion. On the other hand, the dynamics in the detection area captured by $m_y^d = \frac{\langle M_y \rangle_{\mathrm{detection}}}{M_0}$ [see Figs. 3(b) and 3(c)] show oscillations at a frequency close to the frequency of ferromagnetic resonance (FMR):

$$\omega_0 = 2\pi f_0 = \sqrt{\omega_H[\omega_H + \omega_M(j)]}, \tag{2}$$

where $\omega_H = \gamma \mu_0 H$ and $\omega_M(j) = \gamma \mu_0 M_0(j)$ [43]. When increasing the current density, the number of simultaneously existing bullets in the injection area increases, as Fig. 2(c) illustrates. Simultaneously, their frequency f_b decreases, as shown in Fig. 3(c). This downshift in frequency is well known for bullets in in-plane magnetized magnetic films. In the detection area, the frequency f_0 of the dominating FMR mode follows the thermally driven decrease of the magnetization due to Joule heating [for a plot of Eq. (2), see the green dashed line in Fig. 3(d)]. When reversing the current polarity, the dynamics in the injection and in the detection area are progressively suppressed and dominated by the FMR mode, as demonstrated by the good agreement of the spectral maxima with the calculated dependence of the FMR frequency f_0 on j shown in Figs. 3(c) and 3(d).

The emergence of the bullets in the injection area can be characterized by an order parameter

$$\Psi = \frac{1 - m_x^i}{2}, \tag{3}$$

where $m_x^i = \frac{\langle M_x \rangle_i}{M_0}$. The order parameter Ψ in essence captures how far the magnetization deviates from the equilibrium orientation in the absence of a spin current, when $\mathbf{M} \| \mathbf{H}$. Figure 4 shows a plot of the dependence of Ψ on j. One can see a quick initial growth, followed by an intermediate slowing down, which then speeds up again to reach values $\Psi > 0.5$. Let us take a closer look at the initial growth. For a continuous phase transition one can expect, according to Landau [44], a generic dependence

$$\Psi = \left(\frac{j}{j_{\mathrm{th}}} - 1\right)^{\varepsilon} = \Gamma^{\varepsilon}. \tag{4}$$

Indeed, fitting Eq. (4) to the data yields a critical exponent of $\varepsilon = 0.72(3)$ and a threshold current density of $j_{\mathrm{th}} = 0.17(1) \times 10^{11}\,\mathrm{A/m^2}$ (see also the inset in Fig. 4). Figure 4 clearly shows that, at around $\Gamma = 32$, further evolution of the order parameter deviates from Eq. (4). Indeed, the order parameter soon exceeds $\Psi = 0.5$, which implies that, on average, the magnetization is aligned antiparallel to the external field. Before this switching is completely achieved,

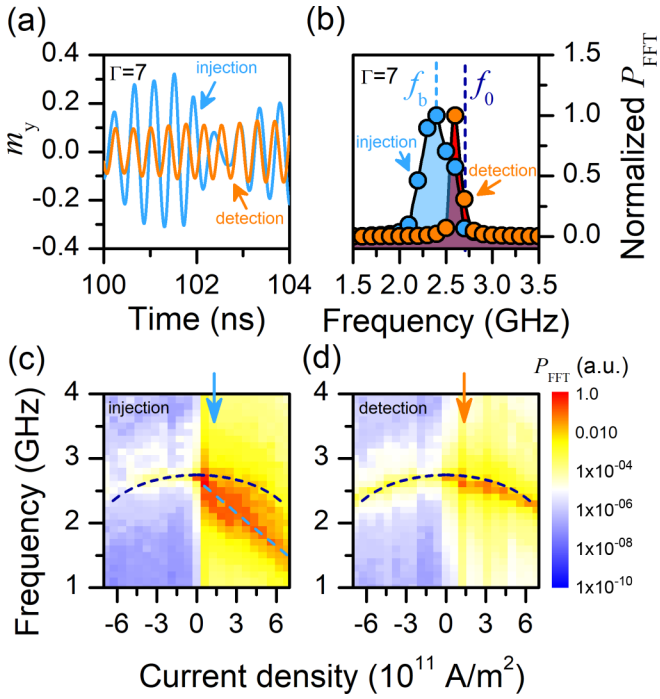

FIG. 3. Spectral characterization of dynamics in the injection and detection area. (a) Part of the typical transient dynamics in terms of the magnetic component m_y^i (m_y^d), spatially averaged over the injection (detection) area, obtained at $\Gamma = 7$. (b) Corresponding Fourier power spectra calculated from a 50-ns-long transient. It features a dominant peak at frequency f_b, marked by the vertical light blue dashed line (close to the frequency of ferromagnetic resonance f_0, marked by the vertical dark blue dashed line). (c) and (d) Dependency of power spectra in the injection and detection areas on the current density. The dark blue dashed line marks the calculated $f_0(j)$. The light blue dashed line serves as a guide to the eye for $f_b(j)$. Blue and orange arrows indicate the spectra shown in (b).

a quasistatic magnetic texture emerges [see Fig. 2(e)]. The spin-torque-induced magnon emission from the injection area can be captured by

$$\Sigma(j) = \langle M_x(j_s = 0)\rangle_d^2 - \langle M_x(j)\rangle_d^2, \tag{5}$$

where the spatial average across the detection area $\langle M_x(j_s = 0)\rangle_d$ refers to a simulation conducted at finite temperature $T(j)$, as caused by Joule heating, but without taking into account the spin current j_s flowing from the Pt stripe into the YIG film. In contrast, $\langle M_x(j)\rangle_d$ refers to a simulation including the action of the spin current. By construction, Σ is proportional to the number of magnons emitted from the injection area, which are caused by only the spin injection, without compromising the thermal background. The current dependence $\Sigma(j)$ is included in Fig. 4. It displays a quick initial growth, followed by a saturation around $\Gamma = 30$. Thereafter, Σ quickly decreases to zero emission.

B. Unrestricted spin-current injection

In this section, the situation sketched in Fig. 2(g) is analyzed, where no spatial restrictions are imposed on the spin-current injection [see Figs. 2(g) to 2(l) for typical snapshots]. Also here, spin-wave bullets appear, although chaos

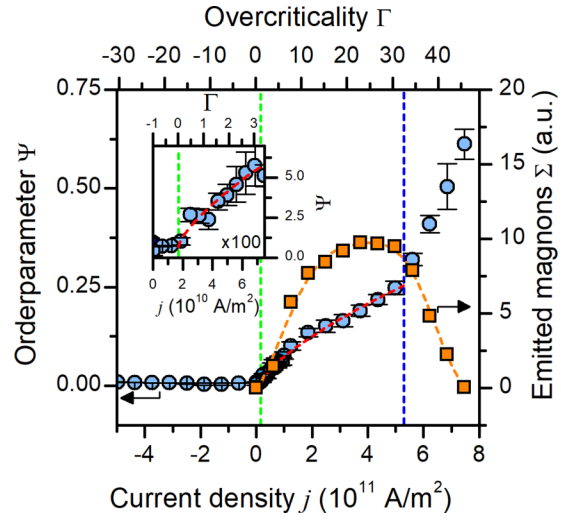

FIG. 4. Dependence of the order parameter Ψ (blue circles) and of the magnon emission Σ (orange rectangles) on the current density j. The red dashed line is a fit of Eq. (3). The inset magnifies the behavior close to the threshold current density. The vertical green and blue dashed lines mark the onset of spin-wave bullet formation and the emergence of the quasistatic texture, respectively. The orange dashed line is a guide to the eye.

sets in earlier. The motivation for this experiment is to analyze and better understand the transition from bullets to the emergence of the quasistatic stripelike texture. The evolution of this transition is elucidated in Fig. 5 in terms of two-dimensional (2D) spatial and spatiotemporal fast Fourier transform (FFT) power maps $P_{FFT}(k_x, k_y)$ and $P_{FFT}(k_x, f)_{k_y=0}$ of m_z. In the left panel of Fig. 5(a) one can see $P_{FFT}(k_x, k_y)$ of an already chaotic state, obtained at $\Gamma = 1$. The magnetization displays no clear structure, as the quite isotropic Fourier spectrum demonstrates. The agreement between the computed dispersion of plane spin waves [45] with the maxima of the spatiotemporal Fourier spectrum $P_{FFT}(k_x, f)_{k_y=0}$ depicted in the right panel shows that the fluctuations here still correspond mainly to linear spin waves. At $\Gamma = 6.4$ [Fig. 5(b)], short-wavelength fluctuations strongly increase. Second, one can see a signature of the bullets appearing in the spatiotemporal Fourier spectrum. That is, the largest spectral weight appears around $k_x = 0$ at frequencies below the computed spin-wave dispersion (dashed line). This deviation is even more pronounced at $\Gamma = 21$ [see Fig. 5(c)]. At $\Gamma = 43$, the short-wavelength fluctuations are suppressed, and the spectrum displays a peculiar anisotropy, corresponding to the stripelike magnetic texture shown in Fig. 2(k). The static behavior of this state is reflected by the spatiotemporal Fourier spectrum, which shows two maxima at frequency $f = 0$. Now, these maxima cannot be related to linear spin waves at all (dashed white curve).

IV. DISCUSSION

A. Bullet dynamics

In the simulations that consider a spatially restricted spin-current injection, one sees the appearance of localized modes above a current density of $j_{th} = 0.17 \times 10^{11}$ A/m^2.

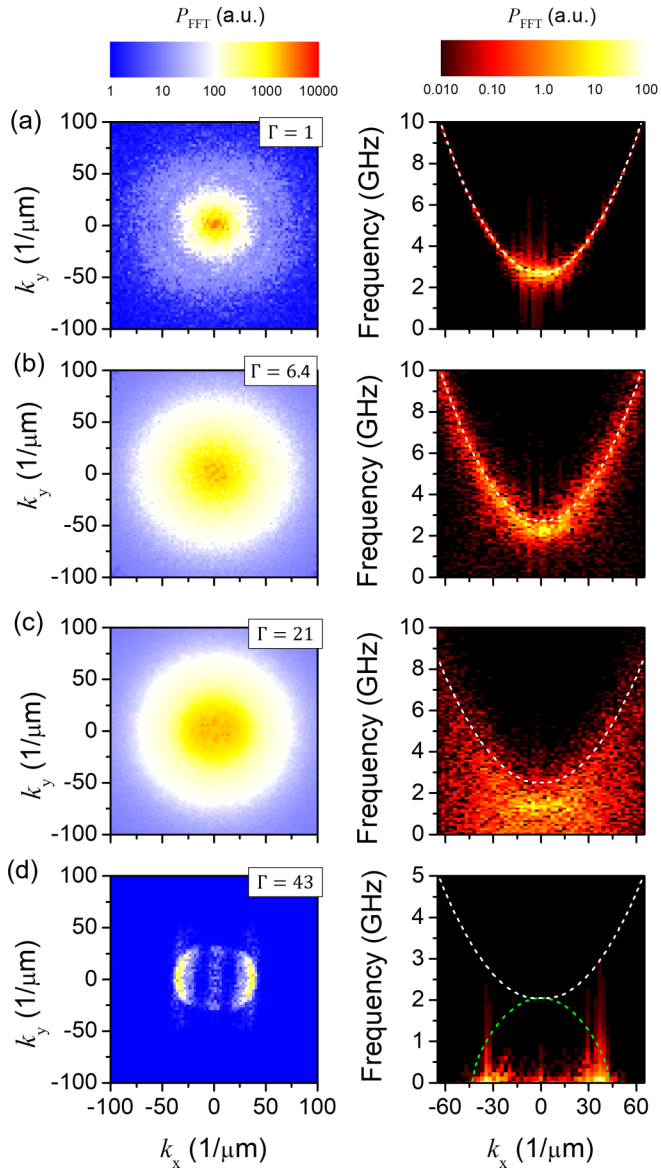

FIG. 5. Spatiotemporal spectral characterization of spin dynamics in the case of unconfined spin injection. The left panels show 2D spatial FFT power maps $P_{FFT}\{m_z(x, y)\}(k_x, k_y)$ of snapshots of the magnetization component m_z. The right panels show spatiotemporal FFT power maps $P_{FFT}(k_x, f)$ along k_x for $k_y = 0$. (a)–(d) refer to specific overcriticalites Γ, as indicated.

This number can be compared with a simple expectation. In the case of YIG nanofilms, the mode with lowest losses is the FMR mode. Without spin currents, its relaxation rate reads [46]

$$\omega_R = \alpha(\omega_H + 0.5\omega_M). \tag{6}$$

The spin torque pumps energy into the magnetic oscillations at a rate [36,37]

$$\beta = j\frac{\gamma\hbar}{2eM_0t_{YIG}}\Theta_{SHE}\tau_i. \tag{7}$$

Exact compensation, that is, $\omega_R = \beta$, leads to a theoretical critical current density of 0.16×10^{11} A/m^2 in the Pt stripe. Only when it exceeds this value can the magnetization become unstable. Indeed, the observed threshold almost exactly coincides with this theoretical expectation. All properties derived from inspecting the current dependency of the dynamics comply with the interpretation that the unstable mode is a spin-wave bullet [42].

B. Turbulence

As more and more bullets appear with increasing current, the dynamics quickly becomes chaotic. Note that this chaos is deterministically driven by the spin-current injection. As a signature of deterministic chaos, I find that, in all spectra discussed in this paper, the phases are random, and they react sensitively to small perturbations of the initial state. This sensitivity is maintained when excluding the thermal fluctuation field.

In the Supplemental Material [38], an analysis of spectral properties of this chaotic state is shown. Chaos appears because, with increasing current, for a larger and larger part of the spin-wave spectrum, losses are compensated. Therefore, dissipation can occur only when three-magnon or higher-order scattering pushes energy into higher-frequency modes, whose losses are not yet compensated by the injected spin current. These nonlinear processes inevitably set in when the unstable modes have achieved large enough amplitudes. Such an energy cascade is, indeed, prototypical for turbulence [47,48]: energy is injected into the low wave number, low-frequency part of the spectrum, and energy is dissipated as it reaches the large wave number, high-frequency part.

Furthermore, there is an interesting connection to classical pipe flow experiments. There, so-called puffs appear as precursors to turbulence [49,50]. At first glance, puffs and bullets seem to have a lot in common, as both appear prior to the onset of turbulence and both dynamics are nonlinear and localized. Similar to the puffs in pipes, the bullets have a finite lifetime. How far does the analogy hold? I would like to emphasize that, in contrast to puffs, the bullets do not move. They remain stationary inside the injection region. Note that this reflects a quite different experimental situation. In pipe flow experiments, one induces turbulence locally by placing objects in the flow or by a nozzle. Here, my focus is on a spatially extended injection region for the spin-current injection, giving rise to chaotic dynamics in this region. The data presented in Fig. 3 show that, outside this region, the magnetic films behave mainly like a normal, thermally excited system. Second, with increasing spin-current injection, turbulence evolves, and the lifetime of the bullets decreases. At even higher current density, the turbulence disappears again, in favor of a quasistatic texture. In contrast, puffs moving downstream have an increasing lifetime as a function of the Reynolds number. As I explain in the Supplemental Material [38], the latter can be regarded as being effectively controlled by the spin-current injection. To further investigate similarities and differences, one could envisage a different sample design, in which the Pt injection stripe consists of two adjacent sections with large and small widths and with a metallic ferromagnetic film below. Then, one can locally induce bullets (= puffs) below the small-width part (= reservoir under pressure). In addition, one may be able to push the bullets into the large-width part

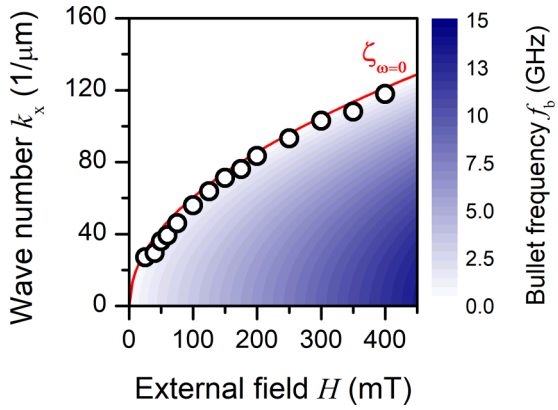

FIG. 6. Field dependence of quasistatic texture. The colored map in the background shows the field and wave number dependence of Eq. (8). The characteristic wave numbers k_0 (open circles) lie on the isocontour $\zeta_{\omega=0}$ (red line).

(= pipe) by means of the spin torque from the current flow inside the ferromagnet, similar to a moving domain wall.

C. Noncollinear spin texture

At larger overcriticality, the progressive softening of the bullet mode culminates in a quasistatic pattern. Note that, besides softening, the local switching of the magnetization also drives the condensation into the stripe pattern: wherever $\mathbf{M}\| - \mathbf{H}$, the injected spin exerts a dampinglike torque. Only at small overcriticality does $\mathbf{M}\|\mathbf{H}$ still hold on average, and the torque is antidampinglike.

Regarding the quasistatic texture, one may recall that Bender *et al.* [32] proposed in 2014 that Bose-Einstein condensation of magnons should set in under spin-current injection. In their theory, a phase diagram was derived under the assumption of small-angle dynamics. Here, I emphasize that, in the case of a strongly excited YIG nanofilm, the nonlinear spin-wave bullets must be considered dynamic modes undergoing condensation. Their local oscillation angle is large. Therefore, the theory of Ref. [32] cannot be applied directly. To further understand the classical condensation phenomenon observed in this micromagnetic simulation work, I suggest first considering the dispersion of bullets, which I here approximate by

$$\omega_b(k) = \sqrt{(\omega_H - a\omega_M k^2)(\omega_H - a\omega_M k^2 + \omega_M)}, \qquad (8)$$

where $a = \frac{2A}{\mu_0 M_0^2}$. Note that in this expression, the wave number $k \propto \frac{1}{d_b}$ characterizes the diameter of the nonpropagating bullet [42]. Comparing the maxima of the Fourier power in Fig. 5(d) with the overlaid dispersion curve Eq. (8) (dashed green line), I find an intersection approximately at the point of vanishing frequency. To rule this out as a mere coincidence, I have repeated the simulations for external fields between $\mu_0 H = 25$ mT and 400 mT. At all fields, I have found at a current density of $j = 7.5 \times 10^{11}$ A/m^2 (corresponding to $\Gamma = 43$) the stripe texture, and I determined the corresponding characteristic wave number k_0. The field dependence of k_0 is plotted in Fig. 6, on top of a colored map encoding the field and wave number dependence of $\omega_b(H, k)$. For all selected fields H, the characteristic wave numbers k_0 lie approximately on the isocontour $\zeta_{\omega=0}$ of vanishing frequency. This reflects the finding that the emerging texture is a quasistatic feature.

Why should this particular mode be chosen? Recall that the conventional dissipation argument for spin-wave instabilities implies that the mode with the smallest losses is selected [17]. For a magnon BEC, this is also the mode with the lowest frequency. Here, this argument fails because the spin torque compensates for the direct dissipative losses. By pushing the bullets as far away from the linear spin-wave spectrum as possible, the system minimizes nonlinear losses that occur because of multiple-magnon scattering. Such processes redistribute energy from the bullets into high-frequency magnons whose losses are not compensated by the spin current. This indirect route remains an active dissipation channel as long as the bullet frequency does not vanish.

V. SUMMARY

The overall picture for spin-current-induced magnetization dynamics in YIG nanofilms obtained from micromagnetic simulation is this: when the threshold current density $j_{\text{th}} = 0.17 \times 10^{11}$ A/m^2 is exceeded, first, single spin-wave bullets appear, whose number quickly increases with increasing current. The bullets then give rise to deterministic chaos. This turbulent state eventually freezes out, in favor of a quasistatic, noncollinear magnetic texture, which finally gradually turns into a completely switched state. Note that combining materials with large spin-Hall angles like β-tungsten [51], with optimally grown YIG nanofilms, displaying Gilbert damping constants as small as only 7×10^{-5} [2,4], opens up a realistic and fruitful perspective for studying samples with large active areas ($w \gg k_b^{-1}$). Then, one might be able to observe turbulent dynamics, as well as the novel, quasistatic texture. While, so far, no experimental reports about the emergence of such a texture exist, the possibility of establishing a connection to experimental work (see the Supplemental Material [38]) further supports this chance. In addition to such experimental opportunities, the findings presented in this paper also open an interesting perspective for the application of spin hydrodynamic theory [52–55]. In particular, at large overcriticalities, the emerging texture breathes at its boundaries, radiating large-amplitude waves (see the video in the Supplemental Material [38]). This process bears similarities to the appearance of dissipative exchange flows discussed in [52].

Finally, I would like to emphasize that the dynamics discussed here are, in particular, rather independent of the actual magnetic material. Qualitatively similar findings can be obtained for metallic ferromagnets like permalloy. Qualitatively different dynamics and textures may emerge in thin films with more complex magnetic anisotropies or antisymmetric exchange.

ACKNOWLEDGMENTS

I acknowledge funding from the Deutsche Forschungsgemeinschaft (DFG, German Research Foundation), 217133147/SFB 1073, project A06, and I thank M. Althammer for helpful discussions.

[1] H. Yu, O. d. Kelly, V. Cros, R. Bernard, P. Bortolotti, A. Anane, F. Brandl, R. Huber, I. Stasinopoulos, and D. Grundler, Sci. Rep. **4**, 6848 (2014).

[2] M. C. Onbasli, A. Kehlberger, D. H. Kim, G. Jakob, M. Kläui, A. V. Chumak, B. Hillebrands, and C. A. Ross, APL Mater. **2**, 106102 (2014).

[3] C. Hahn, V. V. Naletov, G. de Loubens, O. Klein, O. d'Allivy Kelly, A. Anane, R. Bernard, E. Jacquet, P. Bortolotti, V. Cros, J. L. Prieto, and M. Muñoz, Appl. Phys. Lett. **104**, 152410 (2014).

[4] C. Hauser, T. Richter, N. Homonnay, C. Eisenschmidt, M. Qaid, H. Deniz, D. Hesse, M. Sawicki, S. G. Ebbinghaus, and G. Schmidt, Sci. Rep. **6**, 20827 (2016).

[5] G. Schmidt, C. Hauser, P. Trempler, M. Paleschke, and E. T. Papaioannou, Phys. Status Solidi B **257**, 1900644 (2020).

[6] A. A. Serga, A. V. Chumak, and B. Hillebrands, J. Phys. D **43**, 264002 (2010).

[7] A. V. Chumak, V. Vasyuchka, A. Serga, and B. Hillebrands, Nat. Phys. **11**, 453 (2015).

[8] T. Fischer, M. Kewenig, D. A. Bozhko, A. A. Serga, I. I. Syvorotka, F. Ciubotaru, C. Adelmann, B. Hillebrands, and A. V. Chumak, Appl. Phys. Lett. **110**, 152401 (2017).

[9] X.-g. Wang, L. Chotorlishvili, G.-h. Guo, and J. Berakdar, J. Appl. Phys. **124**, 073903 (2018).

[10] B. Heinrich, C. Burrowes, E. Montoya, B. Kardasz, E. Girt, Y.-Y. Song, Y. Sun, and M. Wu, Phys. Rev. Lett. **107**, 066604 (2011).

[11] M. Weiler, M. Althammer, F. D. Czeschka, H. Huebl, M. S. Wagner, M. Opel, I.-M. Imort, G. Reiss, A. Thomas, R. Gross, and S. T. B. Goennenwein, Phys. Rev. Lett. **108**, 106602 (2012).

[12] L. J. Cornelissen, J. Liu, R. A. Duine, J. B. Youssef, and B. J. van Wees, Nat. Phys. **11**, 1022 (2015).

[13] C. Safranski, I. Barsukov, H. K. Lee, T. Schneider, A. A. Jara, A. Smith, H. Chang, K. Lenz, J. Lindner, Y. Tserkovnyak, M. Wu, and I. N. Krivorotov, Nat. Commun. **8**, 117 (2017).

[14] N. Thiery, A. Draveny, V. V. Naletov, L. Vila, J. P. Attané, C. Beigné, G. de Loubens, M. Viret, N. Beaulieu, J. Ben Youssef, V. E. Demidov, S. O. Demokritov, A. N. Slavin, V. S. Tiberkevich, A. Anane, P. Bortolotti, V. Cros, and O. Klein, Phys. Rev. B **97**, 060409(R) (2018).

[15] T. Wimmer, M. Althammer, L. Liensberger, N. Vlietstra, S. Geprägs, M. Weiler, R. Gross, and H. Huebl, Phys. Rev. Lett. **123**, 257201 (2019).

[16] R. Schlitz, T. Helm, M. Lammel, K. Nielsch, A. Erbe, and S. T. B. Goennenwein, Appl. Phys. Lett. **114**, 252401 (2019).

[17] V. S. L'vov, *Wave Turbulence Under Parametric Excitation* (Springer, Berlin, 1994).

[18] N. Bloembergen and R. W. Damon, Phys. Rev. **85**, 699 (1952).

[19] P. W. Anderson and H. Suhl, Phys. Rev. **100**, 1788 (1955).

[20] H. Suhl, J. Phys. Chem. Solids **1**, 209 (1957).

[21] A. V. Nazarov, R. G. Cox, and C. E. Patton, IEEE Trans. Magn. **37**, 2380 (2001).

[22] S. O. Demokritov, V. E. Demidov, O. Dzyapko, G. A. Melkov, A. A. Serga, B. Hillebrands, and A. N. Slavin, Nature (London) **443**, 430 (2006).

[23] A. Rückriegel and P. Kopietz, Phys. Rev. Lett. **115**, 157203 (2015).

[24] J. E. Hirsch, Phys. Rev. Lett. **83**, 1834 (1999).

[25] S. O. Valenzuela and M. Tinkham, Nature (London) **442**, 176 (2006).

[26] A. Hoffmann, IEEE Trans. Magn. **49**, 5172 (2013).

[27] J. Sinova, S. O. Valenzuela, J. Wunderlich, C. H. Back, and T. Jungwirth, Rev. Mod. Phys. **87**, 1213 (2015).

[28] V. E. Demidov, S. Urazhdin, H. Ulrichs, V. Tiberkevich, A. Slavin, D. Baither, G. Schmitz, and S. O. Demokritov, Nat. Mater. **11**, 1028 (2012).

[29] V. E. Demidov, S. Urazhdin, A. Zholud, A. V. Sadovnikov, and S. O. Demokritov, Appl. Phys. Lett. **105**, 172410 (2014).

[30] M. Collet, X. de Milly, O. d'Allivy Kelly, V. V. Naletov, R. Bernard, P. Bortolotti, J. Ben Youssef, V. E. Demidov, S. O. Demokritov, J. L. Prieto, M. Muñoz, V. Cros, A. Anane, G. de Loubens, and O. Klein, Nat. Commun. **7**, 10377 (2016).

[31] V. Lauer, M. Schneider, T. Meyer, T. Brächer, P. Pirro, B. Heinz, F. Heussner, B. Lägel, M. C. Onbasli, C. A. Ross, B. Hillebrands, and A. V. Chumak, IEEE Magn. Lett. **8**, 1 (2017).

[32] S. A. Bender, R. A. Duine, A. Brataas, and Y. Tserkovnyak, Phys. Rev. B **90**, 094409 (2014).

[33] R. E. Troncoso, A. Brataas, and R. A. Duine, Phys. Rev. B **99**, 104426 (2019).

[34] S. O. Demokritov and V. E. Demidov, IEEE Trans. Magn. **44**, 6 (2008).

[35] A. Vansteenkiste, J. Leliaert, M. Dvornik, M. Helsen, F. Garcia-Sanchez, and B. V. Waeyenberge, AIP Adv. **4**, 107133 (2014).

[36] J. Slonczewski, J. Magn. Magn. Mater. **159**, L1 (1996).

[37] H. Ulrichs, V. E. Demidov, and S. O. Demokritov, Appl. Phys. Lett. **104**, 042407 (2014).

[38] See Supplemental Material at http://link.aps.org/supplemental/10.1103/PhysRevB.102.174428 for an example MUMAX3 script file, videos with animated simulation data, as well as additional details about data generation, data processing, the influence of Oersted fields and lateral temperature profiles, connections to experiments, and further characterization of turbulence.

[39] E. E. Anderson, Phys. Rev. **134**, A1581 (1964).

[40] P. Nieves and O. Chubykalo-Fesenko, Phys. Rev. Appl. **5**, 014006 (2016).

[41] U. Atxitia, D. Hinzke, O. Chubykalo-Fesenko, U. Nowak, H. Kachkachi, O. N. Mryasov, R. F. Evans, and R. W. Chantrell, Phys. Rev. B **82**, 134440 (2010).

[42] A. Slavin and V. Tiberkevich, Phys. Rev. Lett. **95**, 237201 (2005).

[43] C. Kittel, Phys. Rev. **73**, 155 (1948).

[44] L. Landau and E. Lifshitz, in *Statistical Physics*, 3rd ed., edited by L. Landau and E. Lifshitz (Butterworth-Heinemann, Oxford, 1980), pp. 446–516.

[45] B. Kalinikos and A. Slavin, J. Phys. C **19**, 7013 (1986).

[46] A. Gurevich and G. Melkov, *Magnetization Oscillations and Waves* (Taylor and Francis, Boca Raton, 1996).

[47] A. Kolmogorov, Dokl. Akad. Nauk SSSR **30**, 301 (1941).

[48] V. Zakharov, V. L'vov, and G. Falkovich, *Kolmogorov Spectra of Turbulence* (Springer, Berlin, 1992), Vol. 1.

[49] I. J. Wygnanski and F. H. Champagne, J. Fluid Mech. **59**, 281 (1973).

[50] K. Avila, D. Moxey, A. de Lozar, M. Avila, D. Barkley, and B. Hof, Science **333**, 192 (2011).

[51] C.-F. Pai, L. Liu, Y. Li, H. W. Tseng, D. C. Ralph, and R. A. Buhrman, Appl. Phys. Lett. **101**, 122404 (2012).

[52] E. Iacocca, T. J. Silva, and M. A. Hoefer, Phys. Rev. B **96**, 134434 (2017).

[53] E. Iacocca, T. J. Silva, and M. A. Hoefer, Phys. Rev. Lett. **118**, 017203 (2017).

[54] E. Iacocca and M. A. Hoefer, Phys. Lett. A **383**, 125858 (2019).

[55] C. Ulloa, A. Tomadin, J. Shan, M. Polini, B. J. van Wees, and R. A. Duine, Phys. Rev. Lett. **123**, 117203 (2019).